

# Robust Numerical Simulation of Porosity Evolution in Chemical Vapor Infiltration

## II. Two-Dimensional Anisotropic Fronts

Shi Jin<sup>\*,1</sup> and Xuelei Wang<sup>†</sup>

<sup>\*</sup>*Department of Mathematics, University of Wisconsin, Madison, Wisconsin 53706; and* <sup>†</sup>*School of Mathematics, Georgia Institute of Technology, Atlanta, Georgia 30332*

E-mail: jin@math.wisc.edu and xwang@math.gatech.edu

Received September 6, 2001; revised March 25, 2002

---

A mathematical model is developed to study formation and evolution of pores during the chemical vapor infiltration (CVI) process. In this model the evolving fiber–gas interface is described by a level-set function with growth rate determined by the vapor precursor concentration and the local geometry. The vapor precursor, solely driven by diffusion, is described by a boundary value problem of the Laplace equation. We then numerically solve this model using the immersed interface method and a fast searching method developed by the authors for pore detection. This model is able to numerically advance the fiber–gas interface and automatically handle fiber merging and pore formation. Numerical experiments are conducted to validate this model and the corresponding numerical algorithm. © 2002 Elsevier Science (USA)

---

### 1. INTRODUCTION

There are a variety of physical phenomena of gas–solid reactions involving porous media. These reactions are accompanied by an increase in volume of the solid phase and by diminishing porosity of the porous medium, due to the formation of a solid product or deposition of a solid species at the gas–solid interface during the process. Gas–solid reactions with solid deposition are exemplified by the fabrication of ceramic matrix composites through the chemical vapor infiltration (CVI) process, during which a matrix of ceramic fibers is chemically vapor deposited within a porous preform. In this paper, we continue our study of the process by building a mathematical model for anisotropic fiber growth rates.

Chemical vapor infiltration is receiving increasing recognition as an important practical approach to fabricating ceramic composites. Among these composites, fiber-reinforced

<sup>1</sup> Research was supported in part by NSF Grant DMS-0196106.

composites (produced by using fibrous preform) are of great technological interest. Because of their improved mechanical properties (high strength-to-density ratio and resistance to fracture) and increasing resistance to oxidation, their use in commercial applications has undergone dramatic expansion over the past decades. The CVI is the most-developed method for fabricating fiber-reinforced ceramic composites [27].

Generally, the CVI process for a fibrous preform can be described as follows. The preform, consisting of a network of reinforcing fibers of carbon or silicon carbide (SiC) arranged in a porous array, is placed in a high-temperature furnace. A vapor precursor of matrix material, such as methyltrichlorosilane (MTS), flowing into the furnace penetrates the pores of the preform. The MTS dissociates at the fiber surface and deposits silicon carbide as a solid coating onto the fiber surface, “growing” the solid fibers and filling the interfiber void. The fibers get larger and the space between fibers becomes smaller. As the deposition process continues, avenues for gas precursor transport become more tortuous and begin to close off. Decreasing porosity makes it possible to form inaccessible pores for gas transport in the course of reaction, and deposition ceases on the fiber surface inside an inaccessible pore (Fig. 1). Eventually the external surface of the preform is completely sealed, preventing further densification of the interior and ending the CVI process. As a final product, the fiber

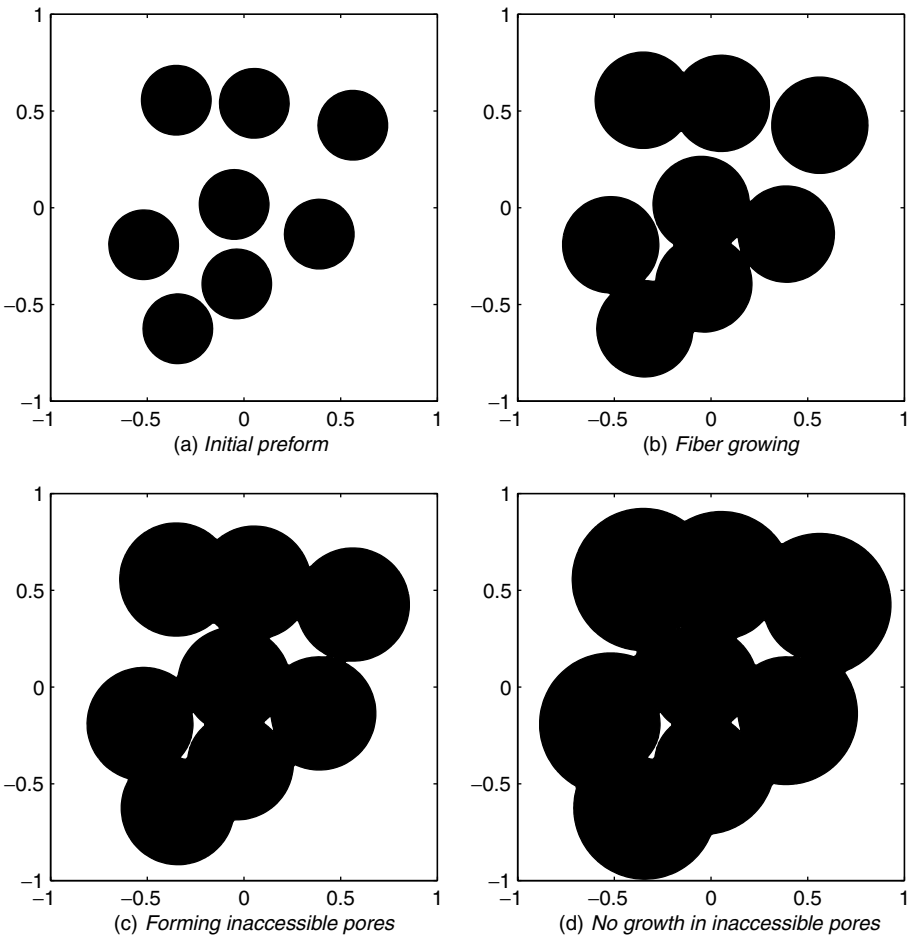


**FIG. 1.** Chemical vapor infiltration process.

coating (also called matrix) interlocks, and the fibers are held together by the coating. This coating along with the fibers constitutes the composites.

Modeling has always played a key role in the development of the CVI process. Mathematical models have been established to study the pore microstructure evolution and to simulate the growth of matrix on fibers. It is natural to use a gas transport reaction equation and/or an equation of conservation of mass [3, 26] to model the mass transport of the reagent to the fiber preform and the deposition kinetics of the solid matrix. But the description of the change of pore microstructure and surface area of the preform as the deposition of matrix occurs is the most difficult part for modeling and simulating the process. The computational difficulty lies in the fact that the pore microstructure may change topology and inaccessible pores may form during the process. Most existing models avoid modeling pore microstructure by modeling the macroscopic quantities, such as porosity, gas permeability, and surface area per unit volume [3, 22, 23], which are quantities dependent on the pore microstructure. Some models assume that inaccessible pores do not take place, which is only valid for the initial stage of the process [21]. Percolation theory may apply but it involves great mathematical and numerical complexity [25]. These models are successful in some aspects, but most of them do not give detailed information about the final pore structure.

The model we proposed in [7, 8], a level-set equation of Hamilton–Jacobi type coupled with a boundary value problem of the Laplace equation, can be used to describe the evolution of pore structures. The main ingredients in this model include the level-set method, a robust numerical technique in capturing the evolving gas–solid interface, and the fast searching method to efficiently detect the inaccessible pores. This model accurately predicts not only the residual porosity but also the close-off time and the shape and location of inaccessible pores, under the assumption that the process is in the kinetic limit where the front speed is a constant unless inside an inaccessible pore.

In general, the ideal condition to achieve the kinetic limit may not be realized in laboratory experiments. Instead, the growth speed of the front may depend on many other factors, such as temperature and its gradient, reagent concentration and its gradient, reaction type, and the local geometry (such as the mean curvature). These variables can affect the ceramic composite structure and properties. In this paper we explore the effect of the reagent concentration and local geometry on the process and final composite structure using an extended model where the growth speed depends on these factors. We also apply an immersed interface method (IIM), derived by LeVeque and Li [11] (and originated from Peskin’s immersed boundary method [18]), for this model. This allows one to solve this complicated front propagation problem with a complex geometry in a Cartesian grid, and an efficient FFT solver can be utilized to optimize the efficiency of the algorithm.

Although this model is phenomenological, it does address some of the main computational challenges in a CVI process, such as the handling of topological changes and pore developments; thus it provides some essential computational tools for realistic simulation of the CVI process.

This paper is organized as follows. In Section 2, we extend our previous model proposed in [7, 8] to include anisotropic front speeds, which depend on the concentration and the local geometry. In Section 3, we outline the numerical approach for the new CVI model. In Section 4, we describe how the immersed interface method (IIM), a numerical technique for solving PDEs with singular sources or in interface problems, is implemented for the new model. In Section 5, we present some numerical experiments on this model, and we conclude the paper in Section 6.

## 2. THE MATHEMATICAL MODEL

### 2.1. Description of the Isothermal CVI (ICVI)

CVI processes can be classified into several types according to (i) whether the preform is uniformly heated and (ii) how the gaseous reagent flows through the preform. The isothermal CVI (ICVI) is one of these variations in current practice and study. In the ICVI, the preform is maintained at a uniform temperature, and the reagent diffuses into the pore space of the preform, reacting on the fiber surface to deposit matrix material (Fig. 2). The ICVI generally requires a long infiltration time since diffusion is slow through the fiber matrix. But it is still frequently used commercially because only simple equipment is required and it can accommodate a large number of different sizes and shapes.

### 2.2. The Setup for the ICVI Model

As in [8], in order to model the evolving process, we take the cross section of a unidirectionally arranged fiber bundle and assume that this cross section is in a rectangular region (Fig. 3). And we use the following notations:

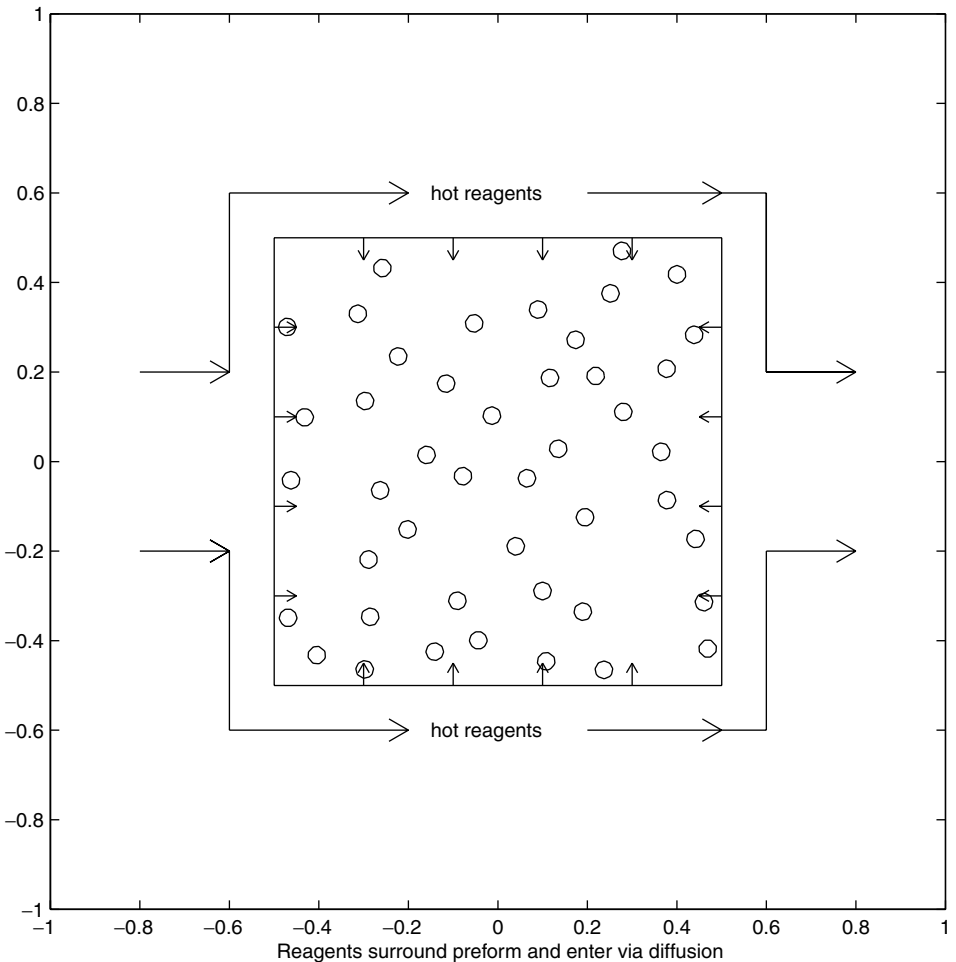


**FIG. 2.** Isothermal chemical vapor infiltration.

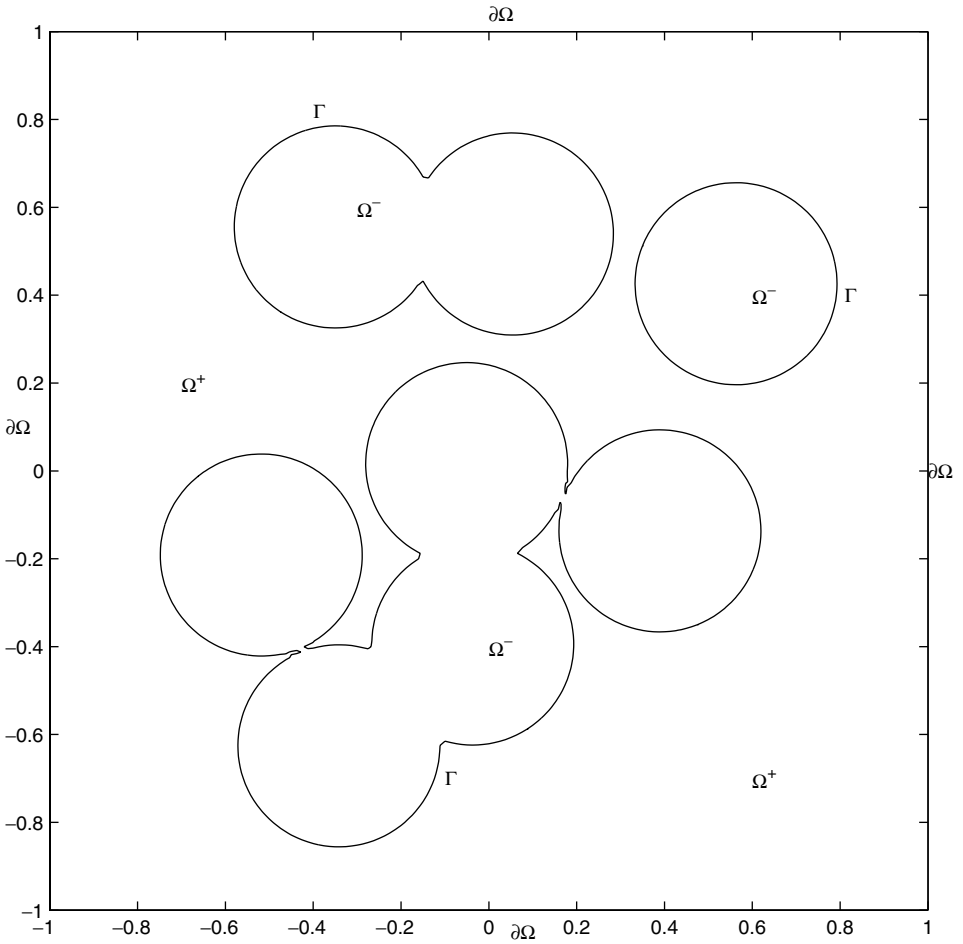


**FIG. 3.** Setup for the isothermal CVI model.

- $\Omega$ , the area where the fibers are placed and grown;
- $\partial\Omega$ , the outer boundary of the problem;
- $\Omega^+$ , the area of gas reagent;
- $\Omega^-$ , the area of developed fibers;
- $\Gamma$ , the interface between fibers and reagent;
- $O$ , the pores inaccessible by reagent from  $\partial\Omega$ .

### 2.3. A Mathematical Model for the ICVI

To describe the ICVI process, the simplest mathematical model requires at least, two partial differential equations. One describes the evolution of the fiber–gas fronts, and the other describes the changes in reactant concentration.

We start with the model developed in [7, 8]. First, the evolution of the fiber–gas front is modeled by a level-set equation of Hamilton–Jacobian type,

$$\begin{cases} \phi_t - c(u, x, t)|\nabla\phi| = 0, \\ \phi|_{t=0} = \phi_0, \end{cases} \quad (1)$$

where  $\phi$  is the level-set function, with  $\Gamma_t = \{x|\phi(x, t) = 0\}$  being the fiber–gas interface at time  $t$  and  $c(u, x, t)$  the moving speed of the interface along the normal direction. The initial value  $\phi_0$  is set to be the signed distance function from  $\Gamma$ .

In the kinetic limit, which occurs under the perfect conditions, the front speed  $c$  is a constant. This was the case studied in [8]. However, in general, other factors, such as temperature, temperature gradient, reagent concentration and its gradient, flow rate, reaction type, and the local geometry, all influence the CVI process. The determination of the deposition and growth rates could be measured by experiments (see [24] for the production of silicon carbide using MTS). Since the temperature in the ICVI process is kept as a constant, we only consider the case where the front speed depends on the concentration gradient and the local mean curvature; namely,

$$\tilde{c}(u, x, t) = K_1 \left( 1 + K_2 \frac{\partial u}{\partial \vec{n}} + K_3 F(\kappa) \right), \quad x \in \Gamma_t, \quad (2)$$

where  $u$  denotes the reactant concentration,  $\vec{n}$  the normal direction, and  $\kappa$  the mean curvature given by

$$\kappa = \nabla \cdot \frac{\nabla \phi}{|\nabla \phi|}. \quad (3)$$

$K_1, K_2, K_3$  are constants that may be determined by experiments [24].

Physically, when an inaccessible pore  $O$  is formed, the fiber front surrounding that area quickly absorbs the reagent remainder and no more reagent is able to reach  $O$ . Thus that part will stop growing, forming a pore permanently. If we take into consideration the accessibility of a point in the region and denote

$$p(x, t) = \begin{cases} 1 & \text{if } x \notin O, \\ 0 & \text{if } x \in O, \end{cases} \quad (4)$$

the normal speed  $c(u, x, t)$  in Eq. (1) is

$$c(u, x, t) = \tilde{c}(u, x, t)p(x, t). \quad (5)$$

The second equation in this model is used to describe the reactant concentration  $u$ . Since the gas is only driven by diffusion, if we assume the concentration is 1 at the outer boundary (gas inlet) and 0 at the fiber front, the following initial and boundary value problem of the heat equation describes the reactant distribution:

$$\begin{cases} u_t - \Delta u = 0 & \text{in } \Omega^+(t), \\ u(x, t) = 1 & \text{on } \partial\Omega, \\ u(x, t) = 0 & \text{on } \Gamma_t. \end{cases} \quad (6)$$

Since the fiber growing speed (millimeters per week) is significantly slower than the gas diffusion, we may assume that the gas phase is always in a steady state. Thus we drop the time dependence in (6) and obtain the Laplace equation for  $u$ . The complete model for the

ICVI process can then be expressed as follows:

$$\begin{cases} \phi_t - c(u, x, t)|\nabla\phi| = 0, \\ c(u, x, t) = p(x, t)K_1\left(1 + K_2\frac{\partial u}{\partial n} + K_3F(\kappa)\right), \\ \phi|_{t=0} = \phi_0, \\ \Delta u = 0 \quad \text{in } \Omega^+(t), \\ u(x, t) = 1 \quad \text{on } \partial\Omega, \\ u(x, t) = 0 \quad \text{on } \Gamma_t. \end{cases} \quad (7)$$

Note that at inaccessible pore area  $O$ ,  $u$  satisfies the Laplace equation with the zero boundary condition on the part of  $\Gamma_t$  that bounds this area; thus the maximum principle implies that  $u \equiv 0$  for  $x \in O$ . Since  $c = 0$  for  $x \in O$ , the fiber surrounding  $O$  ceases to grow, which is exactly what happens physically.

### 3. OUTLINE OF THE NUMERICAL ALGORITHM

The model contains two PDEs. At each time step  $t = t^n$ , the interface  $\Gamma_{t^n}$  is the zero set of the level-set function  $\phi|_{t^n}$ . The boundary value problem of the Laplace equation is solved and its solution  $u|_{t^n}$  is used to determine the moving speed  $c(u^n, x, t^n)$  of the interface. Then we solve the Hamilton–Jacobi equation for  $\phi|_{t^{n+1}}$ . The numerical procedure is as follows.

Initialize the level-set function  $\phi$  to be the signed distance function.

Repeat.

1. From the level-set function  $\phi^n$ , find the necessary interface information, such as the normal and tangential directions, the projections of irregular grid points, and the curvatures.
2. Detect accessibility of all grid points using the fast searching method.
3. Solve the boundary value problem of the Laplace equation for  $u^n$  using the IIM.
4. Calculate the normal speed  $c(u^n, x, t^n)$  of the moving interface.
5. Obtain the level-set function  $\phi^{n+1}$  by solving the Hamilton–Jacobi equation.
6. Go to the next time level until the whole porous region closes off.

As we did in [8], in step 5, the level-set equation is solved by the second-order scheme for convex Hamiltonian introduced by Sethian [19], while in step 2, a fast searching method [8] (which requires  $O(N)$  operations at each step, where  $N$  is the number of grid points) is used to determine inaccessible pores (area  $O$ ). The porosity is computed using the same second-order method as in [8].

In step 3, to solve the Laplace equation in an irregular domain, we use the immersed interface method (IIM) [11] developed by LeVeque and Li. IIM is a difference scheme used to solve the second-order PDEs with discontinuous coefficients and/or singular sources along an irregular interface in a regular domain. Although the interface is moving, the mesh is regular and remains unchanged. The jump condition across the interface is incorporated only into the right-hand side of the discrete equation so that a fast Poisson solver can still be used. The method has a second-order global convergence even though it is only first-order accurate at grid points close to the interface [15].

In the following section, we describe how the IIM is applied to our problem.

#### 4. IMPLEMENTATION OF THE IIM METHOD

The IIM solves PDEs with discontinuous coefficients and/or singular sources along an irregular interface in a simple region by specifying a jump discontinuity in  $u$  and/or its normal derivative  $\frac{\partial u}{\partial n}$ . It uses a uniform rectangular mesh and a modified standard central-difference approximation to achieve second-order accuracy on the grid points far away from the interface and consequently a global second-order convergence. When the coefficients are continuous, it recovers the standard five-point scheme and the specified discontinuity only affects the right-hand side of the discretized equation [11]. As a result, a fast Poisson solver can be used. By using the IIM, the mesh does not change even if the interface is moving. It has been applied to various problems in applications [12, 13, 16].

##### 4.1. The IIM in Two Space Dimension

In this section we outline the IIM for the sake of completeness. This was described in [11]. Experienced readers may skip this section.

Suppose that the problem to be solved is a Poisson equation  $\Delta u = f$ , with  $f$  continuous, in a square region  $[a, b] \times [a, b]$  with suitable boundary conditions. An interface  $\Gamma$  is embedded inside the region and along  $\Gamma$  there are jumps in  $u$  and  $\frac{\partial u}{\partial n}$ . Specifically, the problem is given by

$$\begin{cases} \Delta u = f, \\ [u]|_{\Gamma} = g(s), \\ \left[\frac{\partial u}{\partial n}\right]|_{\Gamma} = v(s), \\ B.C., \end{cases} \quad (8)$$

where  $s$  is the arclength parameter of the interface  $\Gamma$ .

In IIM, a rectangular mesh is used to discretize the Laplace equation (8) in the rectangular domain. Assume a uniform grid is being used:

$$x_i = a + ih, \quad y_j = a + jh, \quad i, j = 0, 1, 2, \dots, n.$$

An IIM can be put into the form of a finite-difference scheme. At grid point  $(x_i, y_j)$ , the scheme has the form

$$\sum_k \gamma_k u_{i+i_k, j+j_k} = f_{ij} + C_{ij}, \quad (9)$$

with  $C_{ij}$  incorporating the boundary conditions at  $\Gamma$ . The sum over  $k$  involves a finite number of points around point  $(x_i, y_j)$ .

First, the grid points are classified into two categories: *regular* points and *irregular* points. A grid point  $(x_i, y_j)$  is a *regular* point if the interface does not cross between any two points of the standard five-point stencil. Otherwise  $(x_i, y_j)$  is an *irregular* point (Fig. 4). At a regular point, (9) is the standard five-point ( $k = 5$ ) approximation,

$$\frac{u_{i+1, j} + u_{i-1, j} + u_{i, j+1} + u_{i, j-1} - 4u_{i, j}}{h^2} = f_{ij},$$

with

$$C_{ij} = 0.$$

The truncation error at a regular point is obviously  $O(h^2)$ .



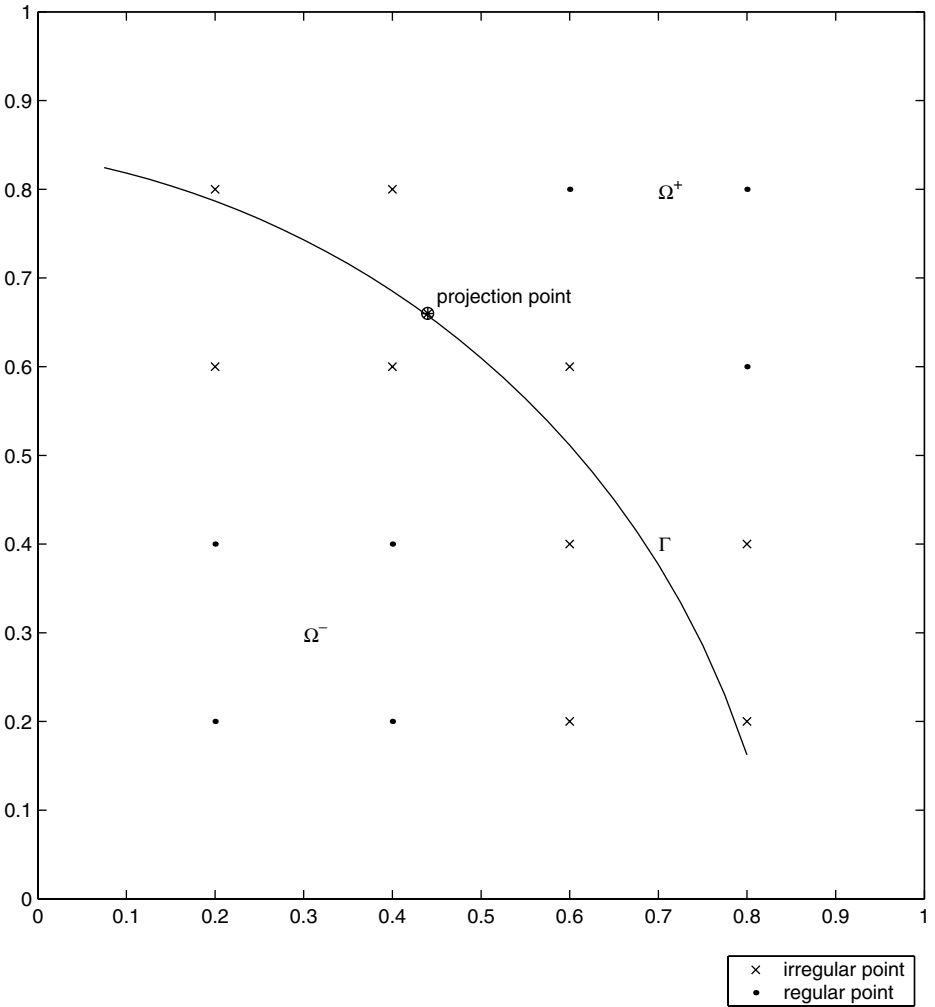


FIG. 4. Irregular and regular points in IIM.

Since the irregular points are adjacent to the interface and form a lower dimensional set, it turns out to be sufficient to require an  $O(h)$  truncation error at these points. In order to determine the difference scheme at an irregular point  $(x_i, y_j)$ , a point on  $\Gamma$  which is close to  $(x_i, y_j)$ , usually the projection  $(x_i^*, y_j^*)$  of  $(x_i, y_j)$  on  $\Gamma$ , is chosen. Then one expands each  $u_{i+i_k, j+j_k}$  at  $(x_i^*, y_j^*)$  by the Taylor expansion using corresponding-limit values of derivatives of  $u$  from the correct side of the interface:

$$\begin{aligned}
 u_{i+i_k, j+j_k} &= u^\pm + u_x^\pm (x_{i+i_k} - x_i^*) + u_y^\pm (y_{j+j_k} - y_j^*) \\
 &\quad + \frac{1}{2} u_{xx}^\pm (x_{i+i_k} - x_i^*)^2 + \frac{1}{2} u_{yy}^\pm (y_{j+j_k} - y_j^*)^2 \\
 &\quad + u_{xy}^\pm (x_{i+i_k} - x_i^*) (y_{j+j_k} - y_j^*) + O(h^3).
 \end{aligned}$$

By doing this one avoids taking derivatives across the interfaces and maintains the desired numerical accuracy of the Taylor expansion.

Using this expansion at each point in the difference equation (9), the local truncation error  $T_{ij}$  can be expressed as a linear combination of the values  $u^\pm, u_x^\pm, u_y^\pm, u_{xx}^\pm, u_{yy}^\pm, u_{xy}^\pm$ . Using the jump conditions across  $\Gamma$ ,

$$u^+ = u^- + g \tag{10}$$

and

$$\frac{\partial u^+}{\partial \bar{n}} = \frac{\partial u^-}{\partial \bar{n}} + v, \tag{11}$$

one can express all values on one side of the interface, say the values  $u^+, u_x^+, u_y^+, u_{xx}^+, u_{yy}^+, u_{xy}^+$ , in terms of the values on the other side,  $u^-, u_x^-, u_y^-, u_{xx}^-, u_{yy}^-, u_{xy}^-$ . This can be done more easily in a local coordinate with directions  $\xi$ , normal to  $\Gamma$ , and  $\eta$ , tangential to  $\Gamma$ .

Once  $T_{ij}$  is expressed as a linear combination of the values  $u^-, u_x^-, u_y^-, u_{xx}^-, u_{yy}^-, u_{xy}^-$ , the coefficient of each of these terms must vanish in order to achieve an  $O(h)$  truncation error. This results in a linear system of six equations to determine the coefficients  $\gamma_k$ . To obtain a solvable system six points are required in the stencil. Normally one uses the standard five-point stencil together with one additional point.

#### 4.2. Application of the IIM to Our Model

In order to use IIM for our problem, first we need to extend the Laplace equation to the whole region  $\Omega$ . We require that  $u$  be continuous along  $\Gamma$ . By the maximum principle,  $u|_\Gamma = 0$  implies that  $u \equiv 0$  in  $\Omega^-$ . So there is an unknown jump discontinuity for normal derivative  $\frac{\partial u}{\partial \bar{n}}$  along the interface  $\Gamma_t$ . By specifying this jump condition  $v(s)$ , we have the equation

$$\begin{cases} \Delta u = 0 & \text{in } \Omega^+(t) \cup \Omega^-(t), \\ u(x, t) = 1 & \text{on } \partial\Omega, \\ [u(x, t)]|_{\Gamma_t} = 0, \\ \left[ \frac{\partial u}{\partial \bar{n}} \right] |_{\Gamma_t} = v(s), \end{cases} \tag{12}$$

where  $v(s)$  is a function of the arc length parameter  $s$  of  $\Gamma_t$ . Since  $u|_{\Gamma^+} = 0$ , (12) implies

$$u(x, t)|_{\Gamma_t^-} = 0. \tag{13}$$

The solution  $u(v)$  of this system is a functional of the jump  $v(s)$  with  $[\frac{\partial u}{\partial \bar{n}}]|_{\Gamma_t} = v(s)$ . To solve the above problem, we are interested in the particular  $v(s)$  such that  $u(v)|_{\Gamma_t} = 0$ . Now, we describe this method in the form of the discretized equation.

#### 4.3. Discretization of the Laplace Equation

Applying the IIM to Eqs. (12) and (13), we obtain

$$LU = F + C, \tag{14}$$

where  $LU = F$  is the discretized form of

$$\begin{cases} \Delta u = 0 & \text{in } \Omega, \\ u(x, t) = 1 & \text{on } \partial\Omega, \end{cases} \tag{15}$$

and  $C$  contains the correction terms. Clearly  $C_{ij} = 0$  for a regular point, while  $C_{ij}$  is a linear combination of  $v$  and  $v'$  at the projection point for an irregular point after taking  $[u]|_{\Gamma_r} = 0$  into account,

#### 4.4. Discretization of the Interface

In order to form the discretized equation of (12) and (13), we need to know the jump values  $v(s)$  of the normal derivative and its derivative  $v'(s)$  at those projections on  $\Gamma$ . We classify those projections into two sets:  $S^+$  is the set of projections of irregular points  $(x_i, y_j)$  outside the interface  $\Gamma_r$ , at which point  $\phi(x_i, y_j) \geq 0$ , and  $S^-$  is the set of projections of irregular points  $(x_i, y_j)$  inside the interface  $\Gamma_r$ , at which point  $\phi(x_i, y_j) < 0$ . We only define the jump values  $v(s)$  at points in  $S^+$ ; the jump values in  $S^-$  and the derivative  $v'(s)$  for both sets are all defined through the interpolation [16]. By doing this, the ill-conditioned equation caused by too many discretization points can be avoided. For any point  $X^*$  on  $\Gamma$ , denote  $\odot$  as those points in  $S^+$  and close to  $X^*$ ; then  $v(X^*)$  and  $v'(X^*)$  can be interpolated as

$$\begin{cases} v(X^*) = \sum_{X_k \in \odot} \alpha_k v(X_k), \\ v'(X^*) = \sum_{X_k \in \odot} \beta_k v'(X_k). \end{cases} \tag{16}$$

Expanding  $v(X_k)$  at  $X^*$  in Taylor expansion along the interface and collecting terms results in a linear system, the solving of which gives the unknown coefficients  $\alpha_k, \beta_k$ . The details of finding projections and interpolation of jump values and their derivatives can be found in [16].

#### 4.5. Discretization of the Residual

We want to find a  $v(s)$  such that the solution of Eq. (12),  $u(v)$ , satisfies the boundary condition  $u|_{\Gamma_r} = 0$ . For an arbitrary  $v$ , the solution usually does not satisfy this condition. To check this condition, one needs to compute the discrete difference of  $u(v)$ , which is called the residual, on the two sides of  $\Gamma_r$ . Namely, one needs to know the residual  $u|_{\Gamma_r^-}$  at those projections in  $S^+$ . Since  $u$  and the jump conditions on  $[u]|_{\Gamma_r}$  and  $[\frac{\partial u}{\partial n}]|_{\Gamma_r}$  are given, we use the weighted least-squares interpolation [14] to find  $u|_{\Gamma_r^-}$  at those projections. This method is used to interpolate  $\frac{\partial u}{\partial n}|_{\Gamma_r^-}$  in [14]. We take exactly the same approach for  $u|_{\Gamma_r^-}$ , i.e.,  $u^- \approx \sum_{i,j} u(x_i, y_j) d_\alpha(|\vec{X} - \vec{x}_{ij}|) - q$ , where  $d_\alpha$  is a cutoff function. Using Taylor expansion of  $u(x_i, y_j)$  at  $\vec{X}$ , collecting terms, and incorporating those jump conditions, we have exactly the same interpolation equation except that the right-hand side of the resulting linear system now is  $(1, 0, 0, 0, 0, 0)^T$  instead of  $(0, 1, 0, 0, 0, 0)^T$  as in [14]; i.e.,

$$\begin{aligned} a_1 + a_2 &= 1, \\ a_3 + a_4 &= 0, \\ a_5 + a_6 &= 0, \\ a_7 + a_8 &= 0, \\ a_9 + a_{10} &= 0, \\ a_{11} + a_{12} &= 0, \end{aligned} \tag{17}$$

where the  $a_k$  are defined the same as in [14].

At each projection,  $u(x_i^*, y_j^*)|_{\Gamma_r^-} = \sum_{i_k, j_k} \alpha_k u(x_{i_k}, y_{j_k}) - q_{ij}$ , where  $q_{ij}$  is a correction term to make the truncation error  $O(h)$ . By considering the jump conditions,  $q_{ij}$  turns out to be linear combinations of  $v$  and  $v'$  at  $(x_i^*, y_j^*)$ . Now we can write the discretized equation for  $u|_{\Gamma^-} = 0$ :

$$EU - Q = 0. \tag{18}$$

We refer the reader to [14] for more details.

#### 4.6. The GMRES Method

Combining Eqs. (14) and (18), we have a discretization of Eq. (12):

$$\begin{cases} LU = F + C, \\ EU - Q = 0. \end{cases} \tag{19}$$

Let  $V$  be the discretization of  $v(s)$  in set  $S^+$ . Since  $C$  and  $Q$  are linear combinations of  $V$  and  $V'$  at each irregular point, where  $C = C(V, V')$ ,  $Q = Q(V, V')$ , and  $V'$  is interpolated from  $V$ , we can write Eq. (19) as

$$\begin{cases} LU = F + BV, & (20a) \\ EU - DV = 0, & (20b) \end{cases}$$

where  $B$  and  $D$  are matrices:  $B$  is the deviation of the difference scheme due to the jump in the solution, and  $D$  is the deviation of the interpolation due to the jump conditions. These matrices are used for theoretical purposes only. In numerical practice, they are never formed explicitly.

Eliminating  $U$  from Eqs. (20), we have

$$(EL^{-1}B - D)V = -EL^{-1}F. \tag{21}$$

Now we can solve this small-size equation for  $V$  using the GMRES method, and then find  $U$  from Eq. (20a).

The main process of the GMRES [4, 5] requires only matrix–vector multiplication. For a linear system  $Ax = b$ , it requires computation of the residual  $r_0 = b - Ax_0$  for an initial guess  $x_0$  and the Arnoldi vectors  $Ar_0, A^2r_0, A^3r_0, \dots$ . When applying GMRES to Eq. (21), where  $A = EL^{-1}B - D$  and  $b = -EL^{-1}F$ , two main procedures are needed: a fast Poisson solver and an interpolation scheme. To compute the initial residual, given an initial guess  $x_0 = V_0|_{S^+}$ , one interpolates  $V_0|_{S^-}$  and  $V_0'|_S$  and then computes  $BV = C = C(V, V')$  and solves Eq. (20a) using a fast Poisson solver for  $U = U_0$ . Thus the residual  $r_0$  can be interpolated from  $U_0$  and by using the jump condition  $V_0$ :  $r_0 = EU_0 - Q(V, V')$ . To compute the matrix–vector multiplication  $AV^+ = (EL^{-1}B - D)V^+$  for a vector  $V^+$ , which corresponds to jump condition on set  $S^+$ ,  $V^+ = V|_{S^+}$ , one interpolates  $V^- = V|_{S^-}$  and  $V'|_S$  and then computes  $BV = C(V, V')$  and  $DV = Q(V, V')$  and uses a fast Poisson solver to compute  $L^{-1}(BV)$ . Consequently,  $AV^+ = E(L^{-1}(BV)) - (DV)$ . Notice that during the process, matrices  $B$  and  $D$  are not computed explicitly.

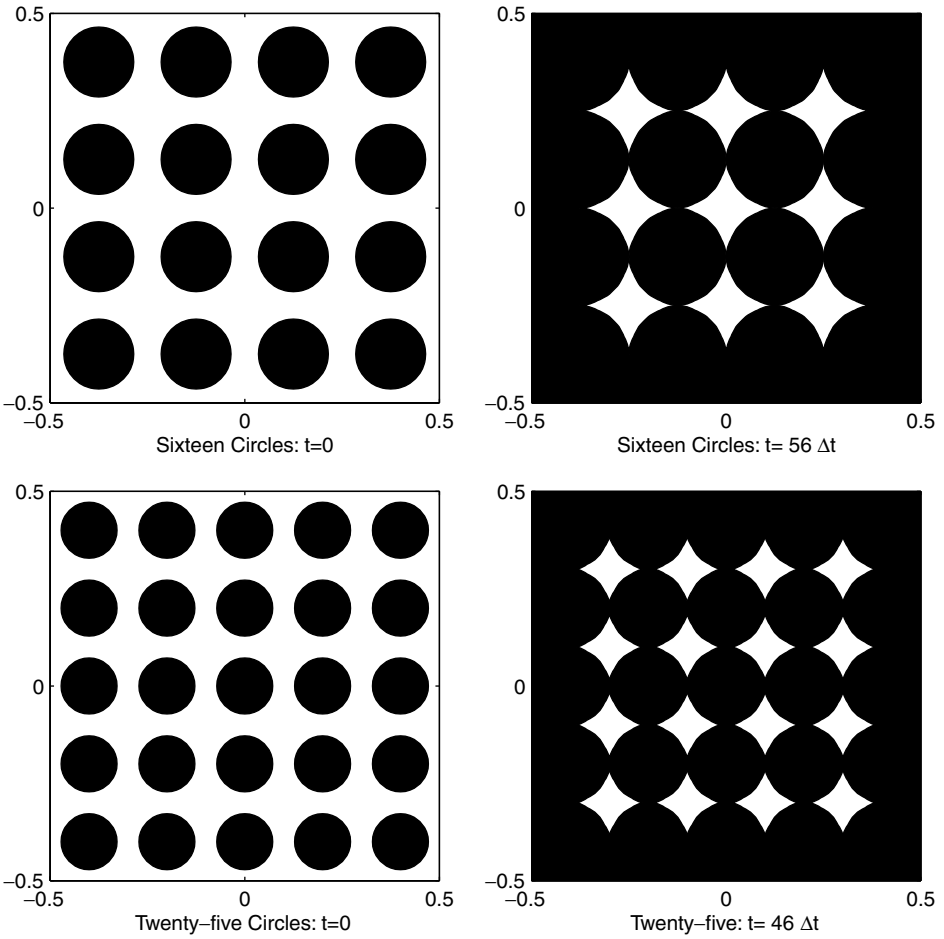


FIG. 5. Square distribution.

## 5. NUMERICAL RESULTS

In this section we present a series of two-dimensional numerical experiments on the pore evolution using our model and the numerical algorithm presented in previous sections.

In all the numerical experiments, all the circles (fiber cross sections) are assumed to be inside a unit-square region. Initially, no circles are allowed to overlay each other or cut across the boundary of the square region. During the process, growing circles may overlay or cross the boundary. For the square initial distribution, the process stops when no growth

**TABLE I**  
**Final Porosity vs Number of Initial Circles: Square Distribution**

Number of initial circles	4	9	16	25
Time steps	115	88	56	46
Final porosity	5.92%	8.58%	13.87%	14.74%

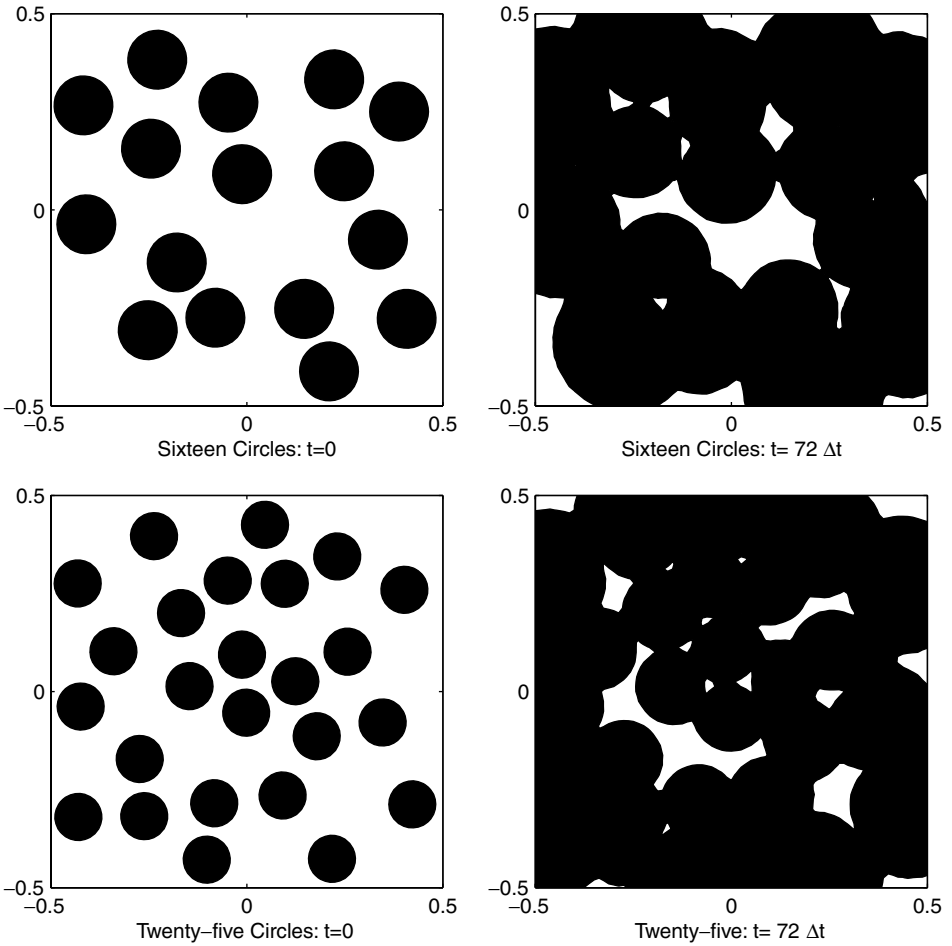


FIG. 6. Random distribution.

can occur inside the unit-square region, but for the random initial distribution, we let the process stop after a fixed number of time steps. The porosity is computed also against this unit square, and the pictures showing the process are drawn only of this region.

In order to avoid the computation complexity as the interface hits the boundary, the computation is carried out over a  $2 \times 2$  square box, with the periodic boundary condition for  $\phi$ . The unit square region is located in the center of the computation domain. And in each space dimension 160 grid points are used (unless otherwise stated), with a proper time step ( $\Delta t = 0.025 \times h$ ) which satisfies the numerical stability condition. For the normal speed of the interface,  $\tilde{c}(u, x, t) = K_1(1 + K_2 \frac{\partial u}{\partial n} + K_3 F(\kappa))$ , we always take  $K_1 = 1.0$  and

**TABLE II**  
**Porosity vs Number of Initial Circles: Random Distribution**

Number of initial circles	4	9	16	25
Time steps	72	72	72	72
Porosity at stopping time	29.90%	12.32%	11.95%	8.97%

$F(\kappa) = \frac{1+|\kappa|}{2+|\kappa|}$ . Since the range of  $\kappa$  is  $[0, \infty)$  due to the formation of the sharp corners, we take a function that can map the range of curvature to  $[0.5, 1)$  and use the constant  $K_3$  to reflect its contribution to the growth. Other constants are specified in each numerical test.

EXAMPLE 1. We consider the following cases of fiber distribution: a bundle of monosize circles are initially distributed on a square lattice, the number of circles being 4, 9, 16, 25,

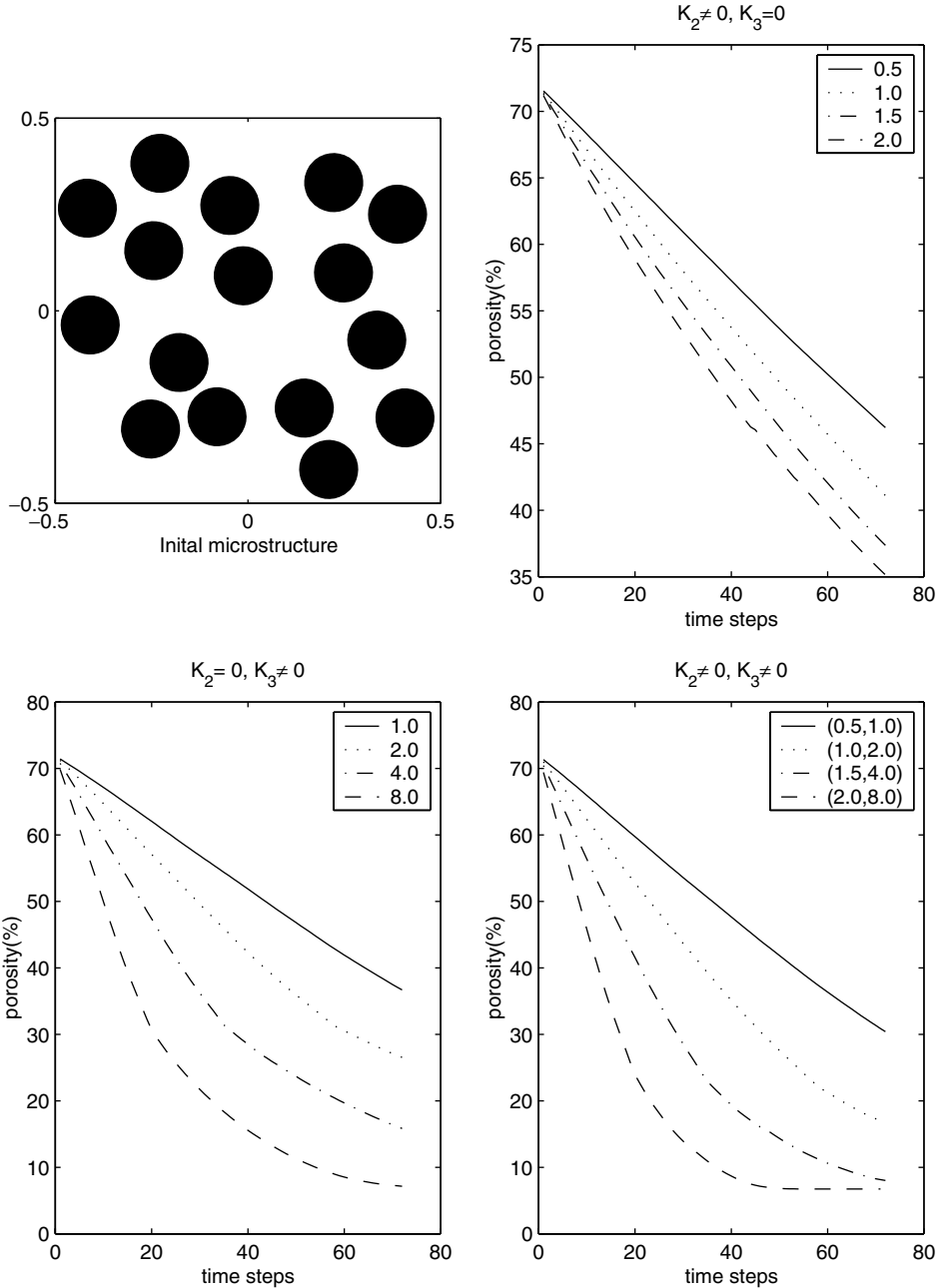
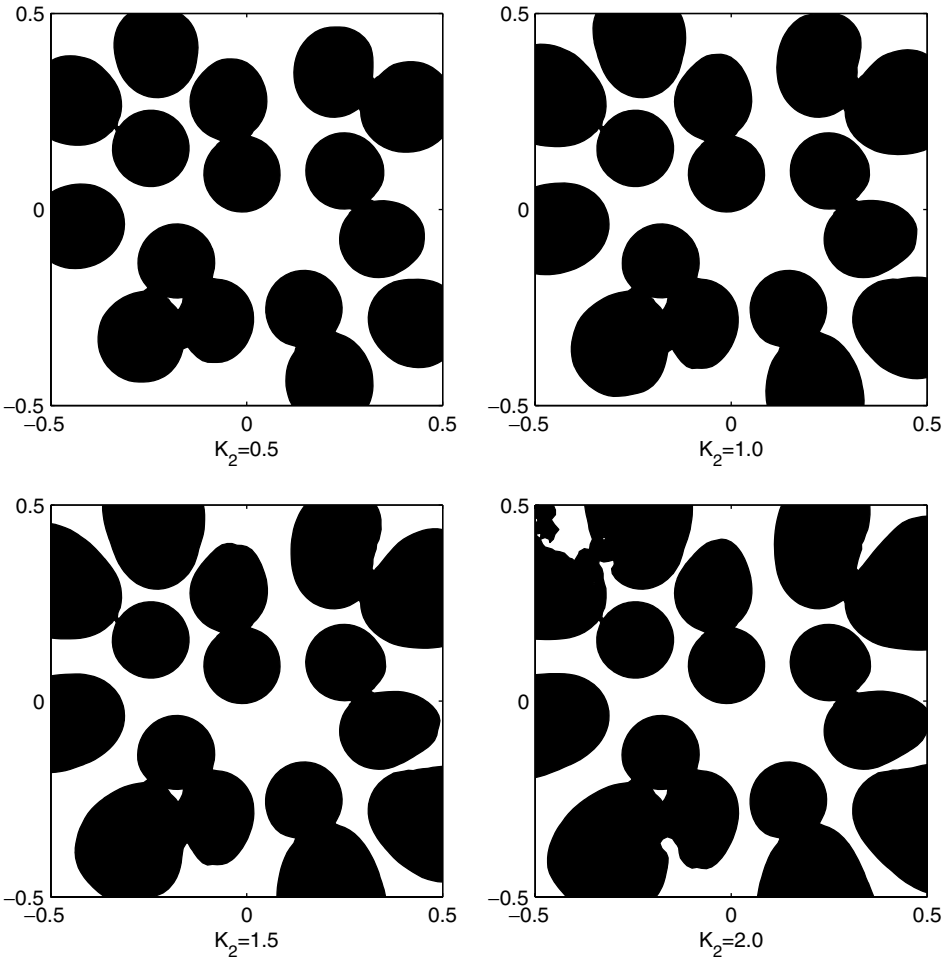


FIG. 7. Initial state and porosity changes for Example 3.

with radius  $\frac{r_0}{2}$ ,  $\frac{r_0}{3}$ ,  $\frac{r_0}{4}$ ,  $\frac{r_0}{5}$ , respectively. Thus in all the cases the initial porosity is the same, being  $P_0 = (1 - \pi r_0^2) \times 100\%$ . Here we take  $r_0 = 0.36$ ; hence  $P_0 = 59.28\%$ . And we also take  $K_2 = 0.5$  and  $K_3 = 4.0$ . See Fig. 5 for the pore evolution with 16 and 25 initial circles, and Table I for final porosity for all cases.

**EXAMPLE 2.** We also test the model for the following fiber distribution. A bundle of monosize circles are initially distributed randomly inside the unit square, with no overlap. As in the previous example, we test different numbers of circles with the same initial porosity, but this time we use  $r_0 = 0.30$ . So the initial porosity is  $(1 - \pi r_0^2) \times 100\% = 71.72\%$ . The parameters for the normal speed are the same as in Example 1 ( $K_2 = 0.5$  and  $K_3 = 4.0$ ). The computations are done only for one instance of the random distribution for each circle number; thus the result for porosity is not an average of several instances. We let the process stop after 72 time steps. See Fig. 6 for the pore evolution with 16 and 25 initial circles, and Table II for the porosity for all the cases at the stopping time.

**EXAMPLE 3.** In the random distribution case, we change the coefficients of the moving speed of the interface to see how this affects the final porosity. We take a random case with



**FIG. 8.** Ending microstructure at  $t = 72\Delta t$  for  $K_3 = 0$ .



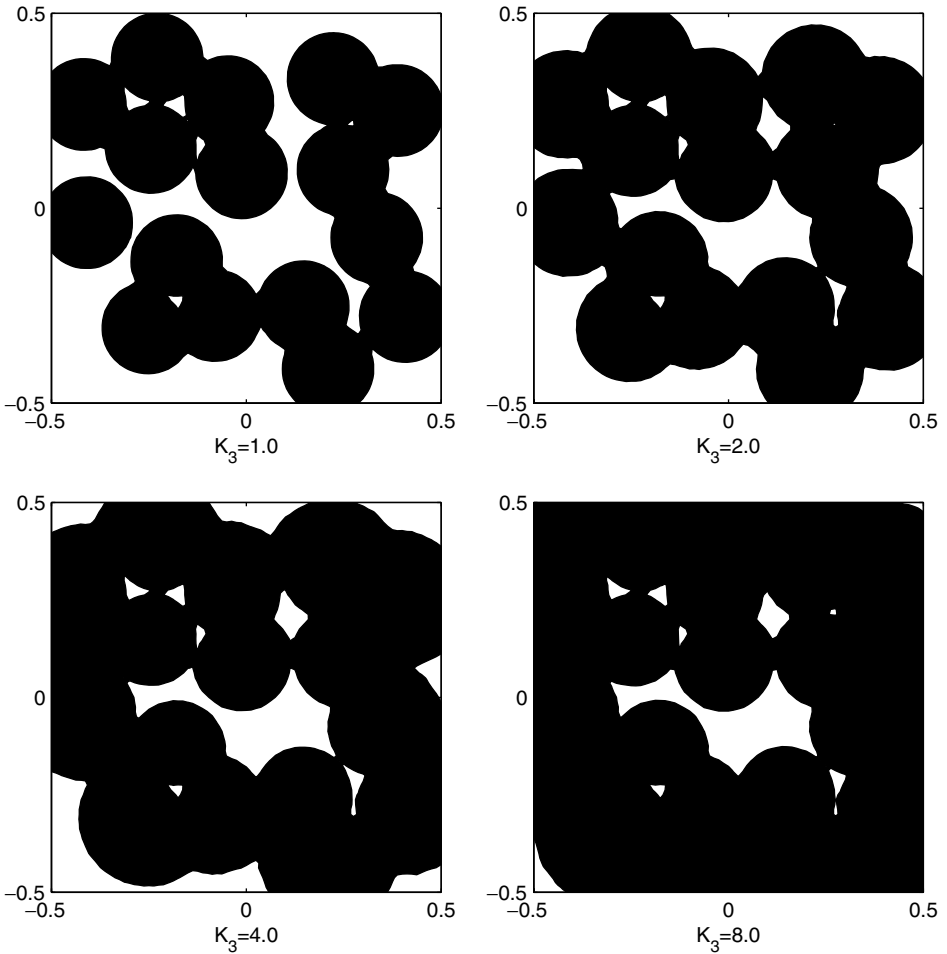


FIG. 9. Ending microstructure at  $t = 72\Delta t$  for  $K_2 = 0$ .

the number of circles = 16. We choose a set of coefficients and try to determine the porosity after 72 time steps. As in the previous example, the result is only for one instance of random distribution. See Fig. 7 for initial state and porosity changes, and see Figs. 8–10 for the pore microstructure at the stopping time (see also Table III).

EXAMPLE 4. As observed in [16], the number of iteration steps of the GMRES is relatively independent of the grid size. To see if that is the case here, for the square distribution with a circle number = 4 and  $K_2 = 1.0$  and  $K_3 = 2.0$ , we change the mesh size to see how it affects the average of the number of iterations. We compute the evolving process for 16 steps in time (for mesh sizes 40, 80, 160, 320 respectively) and record the number of iterations of the GMRES for each time step (see, Fig. 11). The average is shown in Table IV. We see that the average of GMRES iteration steps does not increase too much as the mesh gets finer. The iteration times are higher than those mentioned in the literature [16]. This may be due to the kinks formed around the interface. Notice that the number of GMRES iterations is the same as the number of times the fast Poisson solver is called. So the computation time scales well with the mesh size.

**TABLE III**  
**Porosity vs Moving Speed: Random Distribution**

Coefficient set	Porosity	Stopping time steps
$K_1 = 1.0, K_2 = 0.5, K_3 = 0$	46.21%	72
$K_1 = 1.0, K_2 = 1.0, K_3 = 0$	41.10%	72
$K_1 = 1.0, K_2 = 1.5, K_3 = 0$	37.35%	72
$K_1 = 1.0, K_2 = 2.0, K_3 = 0$	35.31%	72
$K_1 = 1.0, K_2 = 0, K_3 = 2.0$	36.68%	72
$K_1 = 1.0, K_2 = 0, K_3 = 4.0$	26.53%	72
$K_1 = 1.0, K_2 = 0, K_3 = 8.0$	15.84%	72
$K_1 = 1.0, K_2 = 0, K_3 = 16.0$	7.15%	72
$K_1 = 1.0, K_2 = 0.5, K_3 = 2.0$	30.40%	72
$K_1 = 1.0, K_2 = 1.0, K_3 = 4.0$	16.67%	72
$K_1 = 1.0, K_2 = 1.5, K_3 = 8.0$	8.00%	72
$K_1 = 1.0, K_2 = 2.0, K_3 = 16.0$	6.74%	72

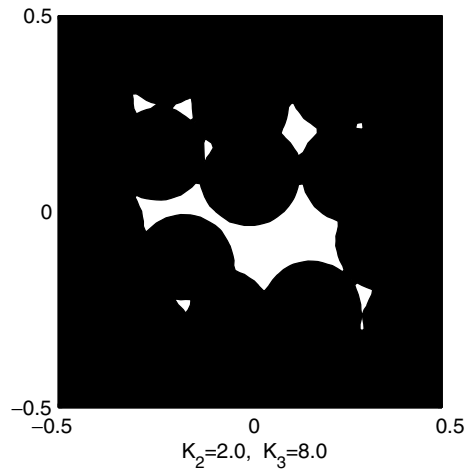
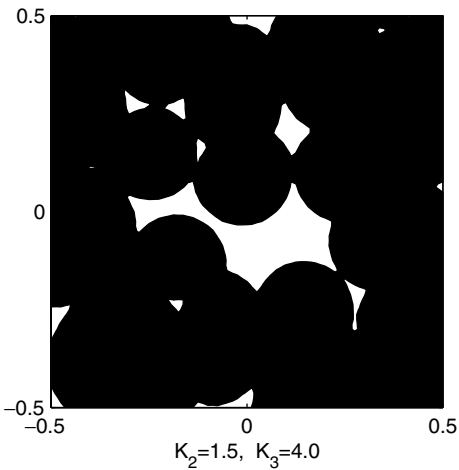
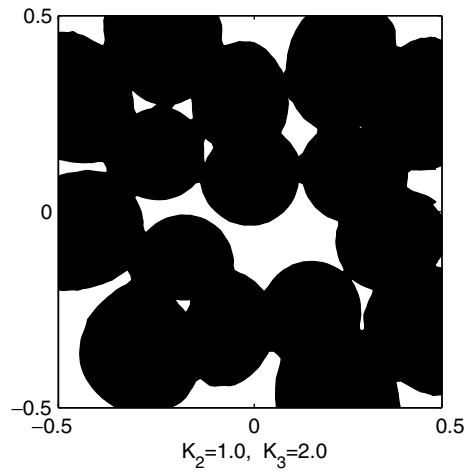
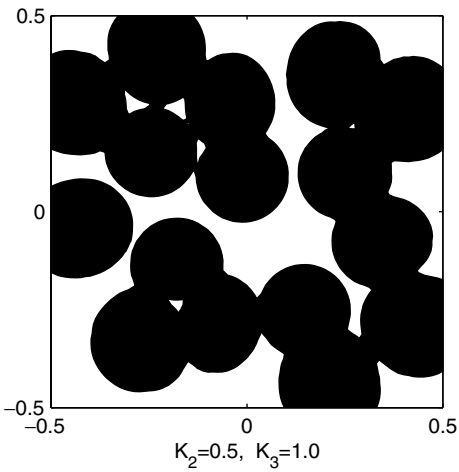


**FIG. 10.** Ending microstructure at  $t = 72\Delta t$  for  $K_2 \neq 0, K_3 \neq 0$ .

**TABLE IV**  
**Iteration Steps vs Mesh Size: Square Distribution**

Mesh size	Evolving steps in time	Average GMRES steps
$40 \times 40$	16	42
$80 \times 80$	16	37
$160 \times 160$	16	42
$320 \times 320$	16	59

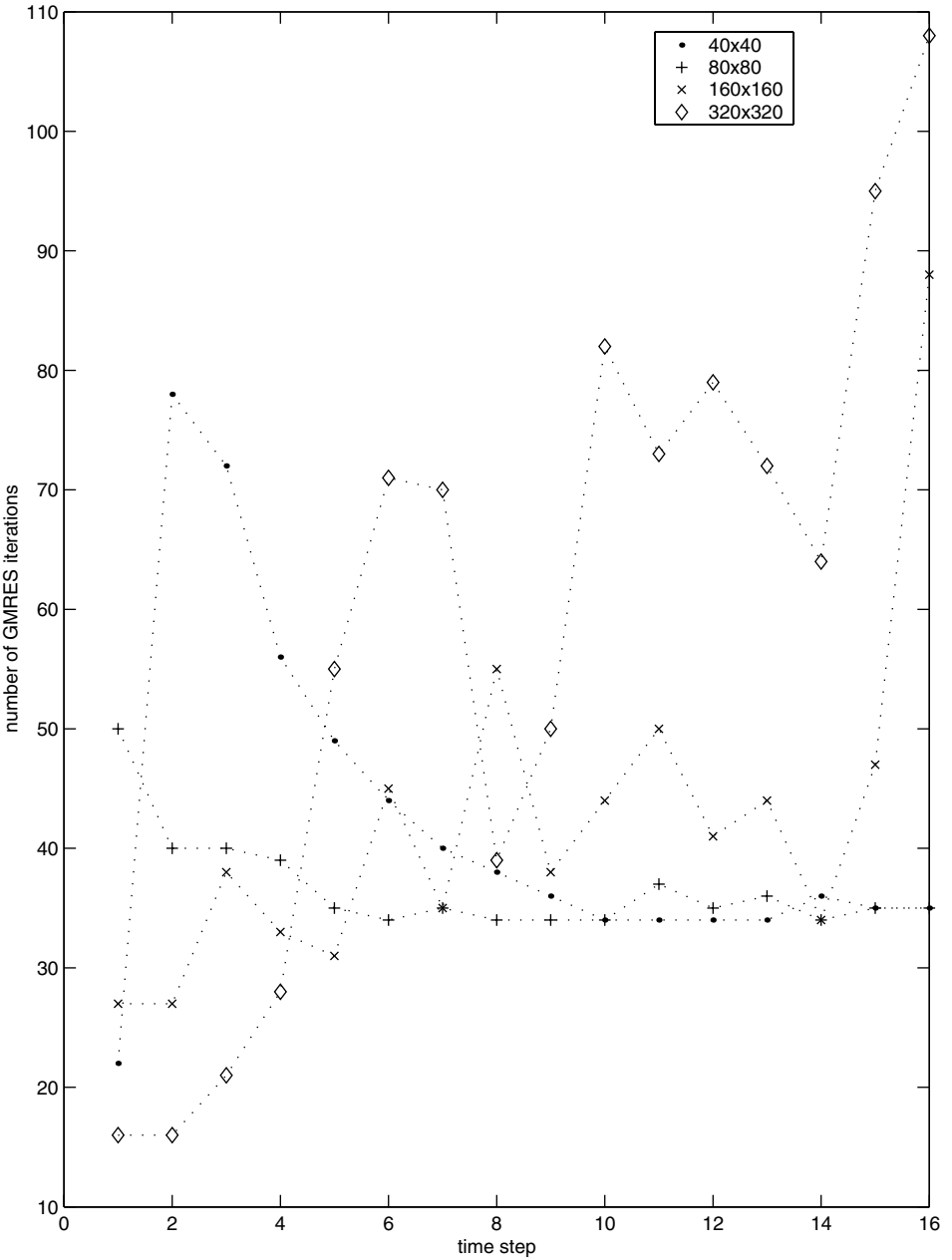


**FIG. 11.** Number of GMRES iterations as mesh refined.

## 6. CONCLUSION

In this paper we introduced a mathematical model for the numerical simulation of the fiber and pore evolution during the isothermal CVI process. In this model, the level-set equation is used to follow the evolving gas–solid interface. We couple the level-set equation with a boundary value problem of the Laplace equation that governs the gas concentration and the formation of inaccessible pores. This Eulerian formulation of the very complex moving interface problem allows the robust capturing of the topological changes, such as the merges of fronts and the formation of inaccessible pores. We use a fast searching method developed in [8] to efficiently detect the inaccessible pore area, and the immersed interface method to solve the underlying Laplace equation in a complex geometry. The numerical results show that the algorithm can effectively evolve the fiber–gas interface and automatically stop fiber growth at inaccessible areas. It gives quantitative predictions on the porosity of the ceramic composite products.

In other types of CVI process, many other factors play a role in the deposit rate and hence affect the distribution of the final pores. This model can be extended without too much effort to include those factors upon suitable incorporation of these factors into the normal speed of the moving interface. This will lead to a deeper understanding and more realistic simulation of the chemical vapor infiltration process and more general gas–solid reaction phenomena.

## ACKNOWLEDGMENTS

We thank Prof. Zhilin Li for providing us with his IIM source code and for numerous discussions about implementation of the IIM method. We also thank Prof. Tom Starr for earlier collaboration on this subject.

## REFERENCES

1. T. M. Besmann, B. W. Sheldon, R. A. Lowden, and D. P. Stinton, Vapor-phase fabrication and properties of continuous-filament ceramic composites, *Science* **253**, 1104 (1991).
2. R. P. Beyer and R. J. LeVeque, Analysis of a one-dimensional model for the immersed boundary method, *SIAM J. Numer. Anal.* **29**, 332 (1992).
3. H. C. Chang, D. Gottlieb, M. Marion, and B. W. Sheldon, Mathematical analysis and optimization of infiltration process, *J. Sci. Comp.* **13**, 303 (1998).
4. J. W. Demmel, *Applied Numerical Linear Algebra* (Soc. for Industr. & Appl. Math., Philadelphia, 1997).
5. A. Greenbaum, *Iterative Methods for Solving Linear Systems* (Soc. for Industr. & Appl. Math., Philadelphia, 1997).
6. J. Hoshen and R. Kopelman, Percolation and cluster distribution. I. Cluster multiple labeling technique and critical concentration algorithm, *Phys. Rev. B* **14**(8), 3438 (1976).
7. S. Jin, X. L. Wang, and T. L. Starr, A model for front evolution with a non-local growth rate, *J. Mater. Res.* **14**, 3829 (1999).
8. S. Jin, X. Wang, T. L. Starr, and X. F. Chen, Robust numerical simulation of porosity evolution in chemical vapor infiltration. I: Two space dimension, *J. Comput. Phys.* **162**, 467 (2000).
9. J. Kinney, T. Breunig, T. Starr, *et al.*, X-ray tomographic study of chemical vapor infiltration processing of ceramic composites, *Science* **260**, 789 (1993).
10. J. H. Kinney, C. Henry, D. L. Haupt, and T. L. Starr, The topology of percolating porosity in woven fiber ceramic matrix composites, *Appl. Composite Mater.* **1**, 325 (1994).
11. R. J. LeVeque and Z. Li, The immersed interface method for elliptic equations with discontinuous coefficients and singular sources, *SIAM J. Numer. Anal.* **31**, 1019 (1994).

12. R. J. LeVeque and Z. Li, Immersed interface method for Stokes flow with elastic boundaries or surface tension, *SIAM J. Sci. Comput.* **18**, 709 (1997).
13. Z. Li, Immersed interface method for moving interface problems, *Numer. Algorithms* **14**, 269 (1997).
14. Z. Li, A fast iterative algorithm for elliptic interface problems, *SIAM J. Numer. Anal.* **35**, 230 (1998).
15. Z. Li and H. Huang, Convergence analysis of the immersed interface method, *IMA, J. Numer. Anal.* **19**, 583 (1999).
16. Z. Li, H. Zhao, and H. Gao, A numerical study of electro-migration voiding by evolving level-set functions on a fixed cartesian grid, *J. Comput. Phys.* **152**, 281 (1999).
17. S. Osher and J. A. Sethian, Fronts propagating with curvature-dependent speed: algorithms based on Hamilton–Jacobi formulations, *J. Comput. Phys.* **78**, 12 (1988).
18. C. S. Peskin, Numerical analysis of blood flow in the heart, *J. Comput. Phys.* **25**, 220 (1977).
19. J. A. Sethian, *Level Set Methods* (Cambridge Univ. Press, Cambridge, UK, 1996).
20. J. A. Sethian, Fast marching methods, *SIAM Rev.* **41**, 199 (1999).
21. B. W. Sheldon and T. M. Besmann, Reaction and diffusion kinetics during the initial stage of isothermal chemical vapor infiltration, *J. Am. Ceram. Soc.* **74**(12), 3046 (1991).
22. D. J. Skamser, D. P. Bentz, R. T. Covrdale, *et al.*, Calculation of the thermal conductivity and gas permeability in a uniaxial bundle of fibers, *J. Am. Ceram. Soc.* **77**(10), 2669 (1994).
23. S. Sotirchos and S. Zarkanitis, A distributed pore size and length model for porous media reacting with diminishing porosity, *Chem. Eng. Sci.* **48**, 1487 (1993).
24. T. L. Starr, Advances in modeling of the chemical vapor infiltration process, *Mater. Res. Soc. Symp. Proc.* **250**, 207 (1992).
25. T. L. Starr, Gas-transport model for chemical-vapor infiltration, *J. Mater. Res.* **10**(9), 2360 (1995).
26. T. L. Starr, A. Smith, T. Besmann, *et al.*, Modeling of chemical vapor infiltration for composite fabrication, in “Sixth European Conference on Computer Material,” p. 231 (Woodhead Publishing Limited, 1999).
27. D. P. Stinton, T. M. Besmann, and R. A. Lowden, Advanced ceramics by chemical vapor deposition techniques, *Ceram. Bull.* **67**, 350 (1988).